THE JOURNAL OF PHYSICAL CHEMISTRY C
A JOURNAL OF THE AMERICAN CHEMICAL SOCIETY

pubs.acs.org/JPCC
Article

Modeling the Shape and Stability of Co Nanoparticles as a Function of Size and Support Interactions through DFT Calculations and Monte Carlo Simulations

Enrico Sireci, Tilman D. Grüger, Philipp N. Plessow, Dmitry I. Sharapa, and Felix Studt*

Cite This: https://doi.org/10.1021/acs.jpcc.5c02777
Read Online

ABSTRACT: In this work, we have employed a combined density functional theory (DFT)-Monte Carlo (MC) approach to produce structural models of Co nanoparticles (NPs), widely employed in the Fischer−Tropsch (FT) synthesis for the production of sustainable aviation fuels (SAFs), in the 2−10 nm size range including the effects of temperature and metal−support interactions (MSI). We make use of a lattice model where the energy of Co atoms is estimated based on their first-shell coordination number (CN), an approach that was validated via DFT calculations. We report a marked increase in step and kink sites at the expense of terraces with increasing particle size, which we linked to the experimentally observed increase in turnover frequency (TOF). Increasing MSI led to a flattening of the NPs on the support as well as to decreasing Co dispersion but hardly affected the site distribution, suggesting that they do not alter the NPs intrinsic activity. We additionally report the size-dependent surface energies and chemical potentials of Co NPs, which are both shown to decrease fast in the 2−6 nm size range and approach convergence afterward. Our models provide a description of these quantities accounting simultaneously for particle size, nonideality of surface morphologies, temperature, and MSI and thus overcome several approximations that previous studies had to rely on.

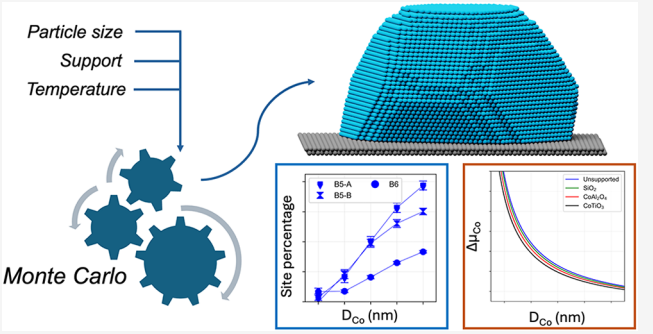

1. INTRODUCTION

The production of sustainable aviation fuels (SAFs) is increasingly coming into focus owing to the fact that the aviation sector currently contributes about 3% of global CO_2 emissions, with demand for aviation fuels projected to increase tremendously.[1] In this context, the synthesis of hydrocarbons from renewable sources (e.g., renewably generated CO and H_2) via, e.g., the Fischer−Tropsch (FT) process, has received widespread attention.

Supported Co catalysts are particularly suitable for the FT synthesis, as they allow for high activity and selectivity toward C_{5+} products at mild temperatures that usually do not exceed 510 K. Structural properties of Co nanoparticles (NPs) at different sizes are important features governing the performance of the catalyst. In fact, while Co NPs larger than 10 nm are generally reported to be structure-insensitive, Co NPs smaller than 10 nm display structure−activity relationships, as in this range, the turnover frequency (TOF) per Co surface area decreases as the particles become smaller.[2−12] Previous computational studies have attempted to clarify this behavior by producing structural models of Co NPs.[13−16] Van Helden et al.[16] developed a Monte Carlo (MC) approach that predicted the equilibrium shape of *fcc*-Co NPs based on the coordination number (CN) of the atoms composing them. Their investigation in the 1−8 nm size range showed that the percentage of step sites, thought to be responsible for CO activation, rapidly increases up to approximately 4 nm, after which it stays constant for the B5-A type and keeps slowly increasing for the B5−B type. The increase in the density of active sites with NP size was thus postulated to be responsible for the size dependency of the TOF of Co catalysts, even though the correlation-breaking point was predicted for a smaller NP diameter than reported experimentally. Very recently, they have extended their approach to the modeling of *hcp*-Co NPs[17] and speculated that the enhanced activity of this crystal phase with respect to *fcc* arises from its greater diversity in terms of sites configuration and to the absence and lower concentration of inactive B4 and 2B3 sites, respectively.

Van Etten et al.[15] elaborated a molecular dynamics (MD) approach to simulate Co NPs equilibrium shapes. They trained a reactive force field (ReaxFF) on an extensive set of Co

Received: April 24, 2025
Revised: June 27, 2025
Accepted: June 27, 2025

https://doi.org/10.1021/acs.jpcc.5c02777
J. Phys. Chem. C XXXX, XXX, XXX−XXX

configurations based on density functional theory (DFT) and applied a simulated annealing procedure to obtain low-energy configurations of Co NPs in the 1−9 nm size range. To predict the size-dependent TOF, they used a microkinetic model that considered the number of sites and the corresponding calculated CO-splitting barriers. The TOF was shown to rapidly increase with NP size up to approximately 5 nm, mirroring the increase in fraction of step sites (in particular *fcc* (110) sites), similarly to the work of van Helden. In later work,[14] they included a fictitious support in the MD runs and investigated its effect with changing metal−support interactions (MSI). Their results showed that the fraction of *fcc* (110) sites was not significantly affected by changing MSI; hence, also the TOF was shown not to change, in agreement with the experimentally observed insensitivity of the size-dependent behavior of the TOF on different supports.[18] Besides these works, numerous other studies have been devoted to the broader topic of metal nanoparticles modeling for catalysis applications.[19−23]

In this work, we employed a paired DFT-MC approach to obtain the low-energy configurations of supported and unsupported *fcc*-Co NPs. We make use of a lattice model similar to the one developed by van Helden et al., where the energy of Co atoms is estimated based on surface energies and their correlation to CN,[24] which is similar to a broken-bond (BB) model.[25] DFT calculations were employed to estimate the energy of Co atoms with changing CN and adhesion energies (γ_{adh}) of Co on α-SiO_2, TiO_2, and γ-Al_2O_3, which have been used as model systems. We developed a Monte Carlo (MC) algorithm that allows to simulate NPs up to the size of 10 nm and includes the influence of the metal oxide support. Using our simulations allowed us to perform a site distribution analysis of the NPs models that have implications for catalyst activity. Lastly, we estimated their size-dependent stability and surface energies. We chose the *fcc*-Co lattice as this is predominantly present for smaller particles,[26] but note that our approach will be easily transferable to the *hcp* phase as well, which will be the subject of future work.

2. COMPUTATIONAL METHODS

2.1. DFT Calculations. Spin-polarized DFT calculations were performed within the software VASP version 6.2[27,28] employing the GGA functional BEEF-vdW[29] and using the projector-augmented wave (PAW) method with standard PAW potentials.[30] Gaussian smearing with a width of 0.1 eV was used in all calculations and the sampling of the Brillouin zone was carried out in a Monkhorst−Pack grid with a k-points linear spacing of approximately 1.78 $Å^{-1}$, that is a (14 × 14 × 1) grid for the (1 × 1) *fcc*-Co (111) surface. Bulk calculations were carried out with an energy cutoff of 600 eV, which was changed to 400 eV for all of the other calculations. Convergence of the SCF cycle was set at an energy difference of 10^{-6} eV, while ionic convergence was achieved when atomic forces were below 0.01 eV/ Å. The convergence threshold of the SCF cycle was reduced to 1×10^{-5} eV for the single-point (SP) calculations carried out for the small NPs models.

Surface energies were calculated by relaxing slab models from 8 to 10 layers thick and applying the following equation

$$\gamma_{(hkl)} = \frac{(E_{slab} - nE_{bulk})}{2A} \quad (1)$$

where E_{slab}, n, A, and E_{bulk} are the energy of the slab, the number of layers, the surface area, and the energy of a bulk Co atom, respectively. The latter quantity was obtained through linear regression of E_{slab} vs n, since, as described elsewhere,[31] this approach ensures high accuracy and fast convergence of the surface energy. As shown in Section S1, all of the surface energies are well converged with slab thickness. The γ_{adh} values between the metal and the support slabs were calculated to mimic the interactions between Co and the different supports. We chose the (111) surface to model the Co slab, as this is by far the most stable facet in the crystal and thus more likely to be found at the interface. To validate this, we computed γ_{adh} for Co (100) on SiO_2 and found that, with respect to the Co (111)−SiO_2 interface, it is stronger by 10 meV/$Å^2$, which is only ∼40% of the surface energy difference (26 meV/$Å^2$) between the two Co facets and thus not enough to make the interface with Co (100) more favorable. Furthermore, we show in Table S13 that the MC-predicted energies of Co NPs on SiO_2 are systematically larger when they expose at the support interface the (100) instead of the (111) facet, thus confirming that the latter configuration is overall more favorable. We calculated γ_{adh} = −103, −74, and −41 meV/$Å^2$ for the Co-$CoTiO_3$, Co-$CoAl_2O_4$, and Co-SiO_2 interfaces, respectively, under the assumption of Co-support compounds formation at the Co interfaces with TiO_2 and γ-Al_2O_3. This assumption is supported by our calculations of Gibbs free energy of formations (ΔG^f) of Co-support compounds shown in Table S5, as well as by previous experimental studies.[32,33] We calculated the ΔG^f under FT conditions of the Co-support compounds as follows

$$\Delta G_f = E_{Co_xMe_yO_{z+x}} + x\mu_{H_2} - xE_{Co^0} - x\mu_{H_2O} - E_{Me_yO_z} \quad (2)$$

where $E_{Co_xMe_yO_{z+x}}$, E_{Co^0}, and $E_{Me_yO_z}$ are the DFT-calculated potential energies of the bulk metal−support compound, bulk *fcc*-Co, and bulk support, respectively, while μ_{H_2} and μ_{H_2O} are the chemical potentials of H_2 and H_2O, respectively. Co^{II} ions in $CoTiO_3$, $CoAl_2O_4$, and Co_2SiO_4 considered in the DFT calculations of γ_{adh} were treated with the Hubbard correction in the rotationally invariant approach introduced by Dudarev et al.[34] with U_{eff} = 1.7 eV. It is worth noting that for the γ_{adh} calculations, we have always considered the interface between Co^0 and the different supports, so, e.g., Co^0 at $Co^{II}Al_2O_4$ interface. A visual depiction of the different calculated interface systems is presented in Figure S2. Further details about the choice of U_{eff} and the calculations of ΔG^f of the Co-support mixed oxides are given in Sections S2 and S3, respectively. The employed procedure for the calculations of γ_{adh} was similar to the one described in a previous work by our group,[35] and further details regarding the methodology, supports investigated, and choice of support slabs are given in Section S4. Details about the interface models and all of the calculated γ_{adh} are reported in Table S6. Coordinates in *xyz* format and energies of all of the DFT-calculated structures are provided in a separate file accompanying this article.

2.2. Monte Carlo Simulations. The *fcc*-Co nanoparticles structural models were obtained by the means of a MC algorithm that redistributes a set of atoms placed in a discretized *fcc* 3D grid, similarly to the approach described by van Helden.[16] The energy of the NP is equal to the sum of the energies of the atoms (E_{Co}) that compose it, that are in turn estimated based on their CN. This method, that we hereby name CN model, is described more thoroughly in Section 3.1. Within the present scheme, the CN of an atom is immediately known by considering how many of the neighboring sites in the grid are

https://doi.org/10.1021/acs.jpcc.5c02777
J. Phys. Chem. C XXXX, XXX, XXX−XXX

occupied by other atoms. The general workflow of the algorithm, graphically depicted in Figure 1, is the following:

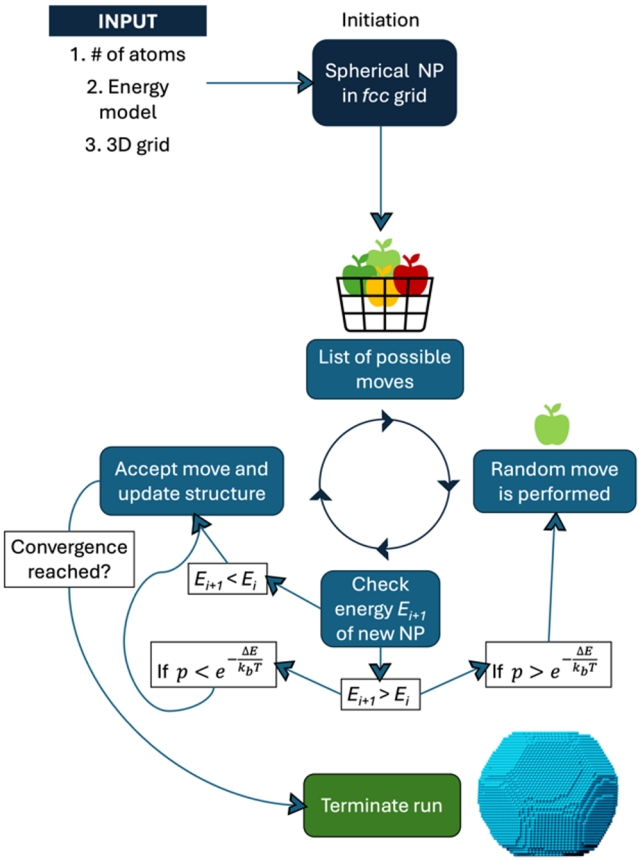

Figure 1. Graphic depiction of the workflow of the Monte Carlo algorithm. p is a random number between 0 and 1.

1. The energy of the structure is evaluated;
2. From a list containing all the possible moves in the system, one is randomly chosen;
3. The energy change resulting from the previously selected move is evaluated;
4. The move is accepted or refused based on the Metropolis criterion (explained below) and the structure is updated accordingly;
5. Points 2 to 4 are repeated until the set number of iterations is carried out.

Each run starts from a spherical arrangement of the atoms, and 5×10^{11} iterations are performed. The Metropolis acceptance criterion used in this work states that a move is always accepted if the energy of the resulting system is lower than the energy of the starting one, while it might be accepted if the final energy is higher based on a Boltzmann probability factor. This expedient allowed us to mimic the effect of temperature on the NPs morphology. The temperature scheme employed in all the runs involved a linear decrease from T = 5000 K to T = 500 K over 90% of the iterations, while a constant temperature of 500 K was kept for the remaining 10% of the run. The high starting temperature allows for fast rearrangement of the atoms from the initial configuration, which is necessary to speed up convergence. We simulated 2 (376 atoms), 4 (3008 atoms), 6 (10152 atoms), 8 (24064 atoms) and 10 nm (47000 atoms) NPs, and the respective number of atoms was chosen as roughly the number of atoms that would fit in a spherical particle of the corresponding size according to the equation below

$$n_{\text{atoms}} = V^{\text{sphere}}(D_{\text{Co}})/V_{\text{m}} \quad (3)$$

where n_{atoms} is the number of atoms considered to reproduce an NP of diameter D_{Co}, V^{sphere} (D_{Co}) is the volume of a sphere with diameter D_{Co}, and V_{m} is the molar volume of Co. We note that for the 2 nm NPs, variations around the chosen n_{atoms} might slightly affect the site distribution since, for this size, even small changes in the number of sites can have a non-negligible effect on the distribution due to the small surface exposed. This translates to a larger uncertainty that is reflected in the relatively large error bars for D_{Co} = 2 nm reported throughout this study. This effect is however expected to become completely negligible for the larger NPs due to the large number of surface sites. In order to obtain a statistically relevant ensemble, 40 independent runs were carried out for each size. The reported site distributions and energies are the average over the 40 lowest-energy structures of these quantities. An extensive statistical analysis of the different ensembles of 40 lowest-energy structures obtained for the unsupported NPs is presented in Section S7. Convergence tests (found in Section S5) were performed on the unsupported 10 nm particles, as these are the largest NPs investigated and thus the ones that are the hardest to converge. These tests showed that both the energy and the site distribution are well converged after 5×10^{11} iterations, which was thus used as threshold for all the other MC runs. The site definition employed in this work followed the scheme proposed by van Hardeveld et al.,[36] and thus we consider 2B3, B4, B5-A, B5−B, and B6 sites, as these are the ones that cover the whole NP surface while maintaining distinct and individually relevant atomic configurations. The different sites are listed in Figure 2.

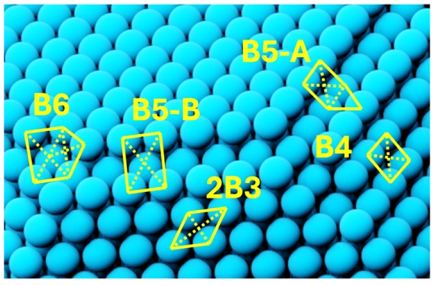

Figure 2. Different atomic arrangements considered in this work are depicted on a Co NP.

The support was included in the simulations as a slab of dummy atoms oriented along the (111) surface in the *fcc* grid; to mimic the stabilization of the NPs due to the presence of the support, the energy of Co atoms in contact with it is reduced by γ_{adh}. Hence, according to the simulation setup, the local environment of the actual Co-support interfaces is not taken into account in the MC runs.

3. RESULTS AND DISCUSSION

3.1. Energy Model and Scaling Relations. In this work, the energy of the NPs was evaluated as the sum of the individual energies of Co atoms (E_{Co}) that compose them. These were calculated based on the Co atom's first-shell CN under the assumption that E_{Co} scales linearly with CN. We herein refer to this energy model as the CN model. The close-packed *fcc* (111)

https://doi.org/10.1021/acs.jpcc.5c02777
J. Phys. Chem. C XXXX, XXX, XXX−XXX

surface is composed of atoms with CN = 9; thus, by calculating $\gamma_{(111)}$, we have obtained the energy difference between a Co atom in the bulk (CN = 12) and one with CN = 9, from which we derived the linear correlation depicted as the dashed blue line in Figure 3. We assigned an artificially high energy to atoms with

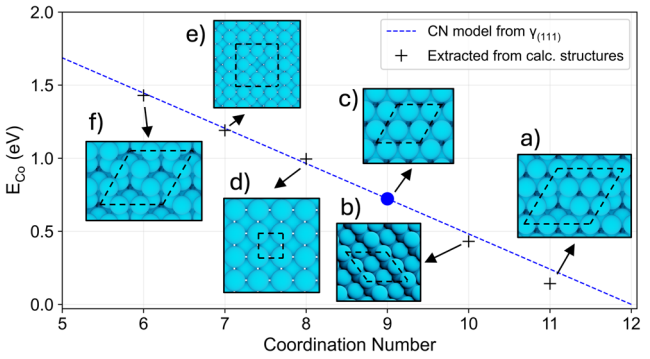

Figure 3. E_{Co} with changing CN as predicted with the CN model and obtained from explicit calculations. The data points were obtained based on the following structures: (a) (111) surface with 1/9 monolayer (ML) vacancy density, (b, c) (111) surface, (d) (100) surface, (e) (100) surface with 1/9 ML vacancy density, and (f) (111) surface with 1/3 ML vacancy density.

CN = 0 to avoid their unphysical detachment from the NP during the initial stages of the simulation. To assess the reliability of this framework, we compared our CN model with the explicitly calculated energies of Co atoms with different CN. These were estimated by calculating the surface energies of the mostly hypothetical structures depicted in Figure 3 and by solving the resulting system of linear equations from which we retrieved the energies of Co atoms with CN = 6, 7, 8, 10, and 11 in addition to CN = 9 and 12. The specifications relative to these structures are given in Table S3. The plot in Figure 3 shows good agreement between the CN model and explicitly calculated E_{Co}, hence confirming that it is adequate to describe the energies of Co atoms in this CN range. We observe that extrapolating the CN energies to CN = 0 would yield a Co sublimation energy of 2.89 eV, significantly lower than the reported experimental value of 4.43 eV.[37] This is not surprising, as the CN model assumes that the metal−metal bonds are characterized by a fixed energy regardless of CN, while it is known that decreasing CN leads to an increase in bond strength.[38,39] Methfessel and Scheffler[39] showed that the E(CN) for different metals can be described accurately by a square-root relation, that is mostly linear down to CN = 5−6 and grows faster with further decrease of CN. This study thus confirms the validity of the CN model for the high CN range that is the one we are concerned about in the present work, since almost all the atoms in the NPs have CN ≥ 6. We note, however, that few Co atoms with CN = 5 appear in some of the NPs models but in a negligible proportion. We verified that the underestimation of the Co sublimation energy is not a feature of the present DFT framework by comparing the energy of bulk Co and an isolated Co atom in the gas phase, which yielded a sublimation energy underestimated by only 3.5% with respect to the experimental value, thus confirming the breakdown of the CN model in the low CN range. Moreover, in Figure 4, we report the parity plots of the MC-predicted against the DFT-calculated energies of an ensemble of 15−20

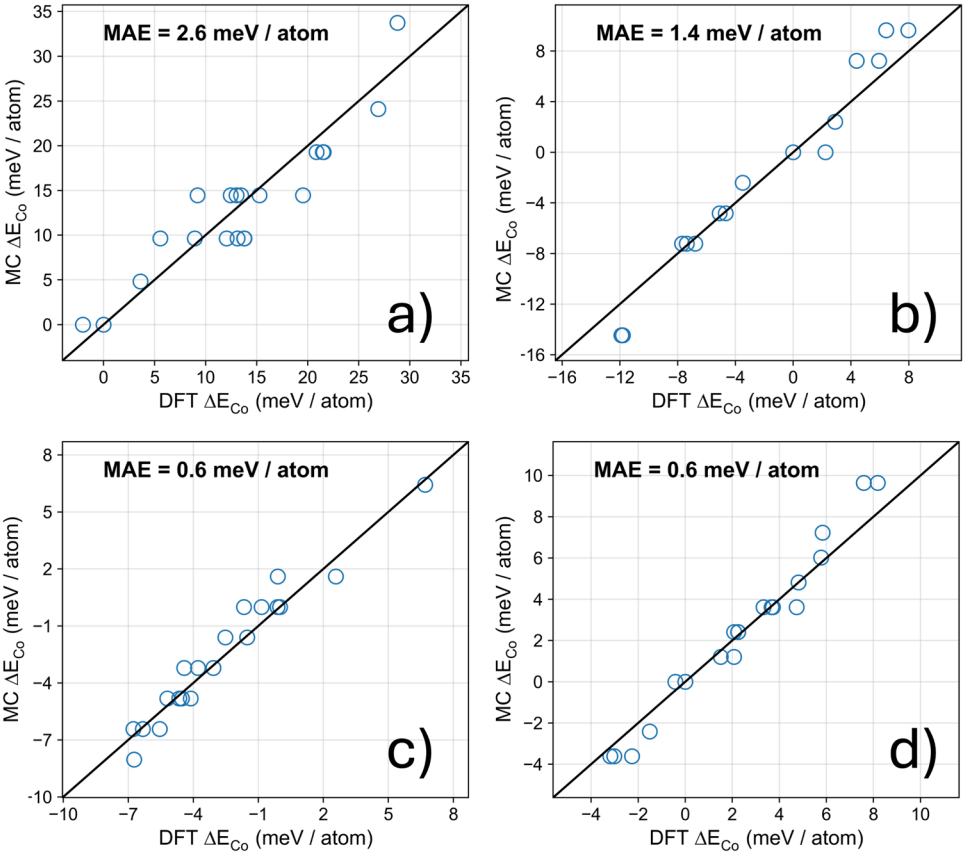

Figure 4. Parity plots of MC vs DFT-calculated ΔE_{Co} of (a) 100, (b) 200, (c) 300, and (d) 400 atom Co NPs obtained from short MC runs.

https://doi.org/10.1021/acs.jpcc.5c02777
J. Phys. Chem. C XXXX, XXX, XXX−XXX

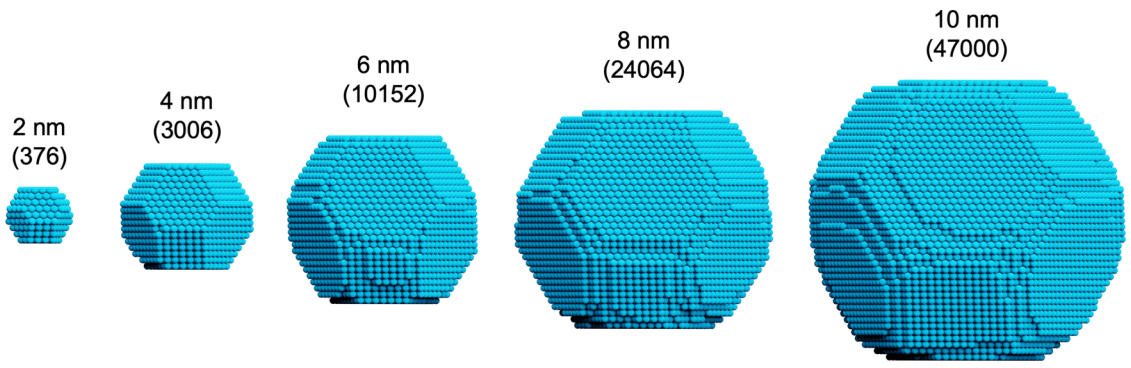

Figure 5. Structural models of Co NPs obtained with the MC algorithm. The number of Co atoms composing the NPs are given in parentheses.

particles containing 100, 200, 300, and 400 Co atoms that are benchmarked against DFT calculations according to the following equation:

$$\Delta E_{\mathrm{Co}}^{\mathrm{DFT}} = E_{\mathrm{NP}x}^{\mathrm{DFT}} - xE_{\mathrm{bulk}} \quad (4)$$

where $\Delta E_{\mathrm{Co}}^{\mathrm{DFT}}$ is the DFT-calculated energy of the NP with respect to bulk Co, $E_{\mathrm{NP}x}^{\mathrm{DFT}}$ is the DFT-calculated potential energy of the NP, x is the number of atoms in the NP, and E_{bulk} is the DFT-calculated energy of one bulk *fcc*-Co atom (see Section S6 for more details). Importantly, our model performs increasingly well with increasing particle size, and already from NPs of 300 atoms, a mean average error of only 0.6 meV/atom is achieved, which is below the typical threshold of machine-learning potentials[40] when compared to DFT, highlighting the very high accuracy achieved with this rather simple model. We additionally report analogous parity plots where the energies are normalized by the number of surface atoms in Figure S4. Also in this case, the MAEs decrease with particle size, and for the 300 and 400 atom NPs, they are only 1.1−1.2 meV/surface atom. We additionally point out that the errors for the practical cases of this study are expected to be even lower, as this benchmark was carried out on NP structures that are relatively far from their equilibrium shapes, for which we expect our CN model to perform better as it was derived from the equilibrium structure of the Co (111) surface.

3.2. Shapes and Site Distribution of Unsupported Co NPs. Snapshots of the converged Co NPs (5×10^{11} MC steps) in the investigated size range are presented in Figure 5 (Figure S13 shows the frontal, side, and top views of these NPs, their *xyz* coordinates, and energies can be found in the SI). All NPs assume a truncated octahedron (TO) shape, where large (111) terraces alternate with smaller (100) ones. We observe that whereas small NPs showcase edges at the intersection between the terraces, in larger NPs these are increasingly substituted by steps, of the B5-A type between (111) and (100) surfaces and of B5−B type between two (111) terraces. The site distribution analysis presented in Figure 6 shows that the B5-A and B5−B step sites are shown to increase almost linearly in the investigated size range, being mostly absent in the 2 nm NPs and peaking at 7.8 and 6.0%, respectively, for the 10 nm particles. We additionally note that the B5-A sites are slightly preferred over the B5−B ones for NPs larger than 6 nm. Besides the emergence of step sites, as the NPs grow bigger, their surfaces become more defective as an increasing number of kinks are detected. This observation can be explained in light of the configurational entropy contribution to the stability of the NPs. In fact, the presence of defects increases the number of possible surface arrangements with a consequent increase of configurational entropy. Regular surfaces are thus characterized by low configurational entropy: this would be 0 in the case of a perfect Wulff crystal, as there is only one possible atomic arrangement that corresponds to this morphology. In order for surface defects to form, the entropic contribution to the stability of the NPs must outweigh the associated energy penalty arising from the formation of the poorly coordinated atoms found at the kinks. As the NPs grow larger, the number of possible surface configurations increases dramatically along with the entropic contribution to their stability, which thus causes an increase of surface defects and irregularities. To prove this statement, we

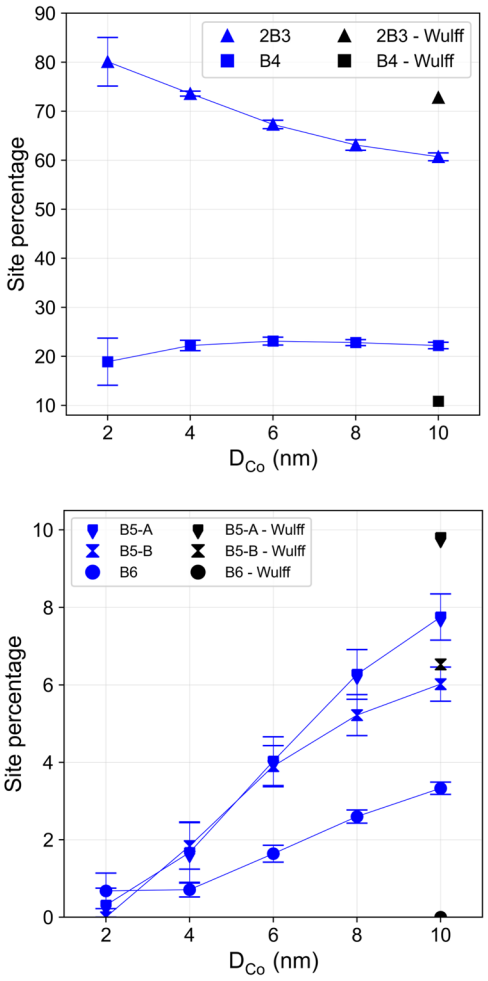

Figure 6. Site distribution analysis of unsupported Co NPs with increasing particle diameter.

https://doi.org/10.1021/acs.jpcc.5c02777
J. Phys. Chem. C XXXX, XXX, XXX−XXX

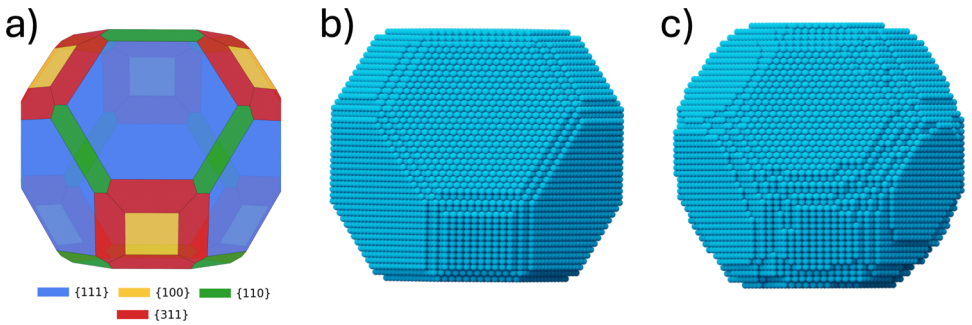

Figure 7. (a) Schematic and (b) atomistic model of a 10 nm fcc-Co Wulff crystal computed based on the DFT-calculated surface energies found in Table S1 and (c) 10 nm Co NP produced via the MC algorithm.

run additional 10^9 MC iterations at T = 500, 1000, 1500, and 2000 K on the global minima previously obtained for the different particle sizes and kept track of the NP energy evolution. Both the energy fluctuations at a given temperature and the overall increase in energy with the temperature reflect the extent of the configurational space explored by the system. These are larger when the configurational entropy is higher. In Figures S11 and S12, we show the NPs energy evolution with number of iterations and the distribution of the sampled energies throughout the MC runs. As expected, with increasing temperature, both the absolute energy increase and the width of the energy distribution increase but, importantly, to a larger extent with increasing particle size. This qualitatively confirms that larger particles have an intrinsically higher configurational entropy, that is likely a reason for the increase in surface defects reported with increasing D_{Co}. A further reason for the increase of B6 sites is that since the majority of these sites are irregularities located on step rows, an increase in number of step sites also leads to an increase of B6 sites. The site distribution in Figure 6 confirms this idea by showing a significant increase, once again close to linear, of B6 sites with increasing NP size. The B5-A, B5−B, and B6 sites increases occur at the expense of 2B3 sites, which decrease from 80.1 to 60.7% in the investigated size range. On the contrary, B4 sites are shown to stay almost constant at about 20%. We note that the relatively large error bars shown in Figure 6 for the 2 nm NPs arise from the fact that, for small particles, small differences in surface configurations lead to proportionally large deviations in site distributions, and not from a larger diversity in the ensemble. In fact, we show in Section S7 that the ensemble of 2 nm NPs is the least energetically and structurally diverse among those investigated.

The implications of these changes in site distribution with growing NP size are often discussed in light of the FT activity of the Co catalysts. Several theoretical studies reported that CO splitting on step and especially kink sites is characterized by lower barriers than on (111) and (100) terraces,[11,41−43] where they are found to be prohibitively high, thus not matching with experimentally observed activation energies for FT. The hereby reported increase of B5-A, B5−B, and B6 sites with increasing size might hence explain the observed size-dependent behavior of the TOF.[11] Similar results were obtained by the previous studies of Van Helden et al. and Van Etten et al., even though in both works the concentration of the alleged active sites was found to converge at NP diameters (D_{Co}) of about 5 nm (with the exception for the B5−B sites in the work by Van Helden, which are shown to keep increasing after this threshold, albeit slowly), while the experimental TOF behavior is characterized by a mostly linear increase up to a plateau at around 10 nm. This experimental trend is well reproduced by our results, further corroborating our methodology. We do not observe, however, the site distribution approaching convergence even at around 10 nm, and the step and kink concentration is expected to keep increasing for D_{Co} > 10 nm. This is not necessarily in disagreement with the experimental TOF behavior, as an increase in active sites does not always translate in increased activity. In fact, recent microkinetic models[44] have shown that this correlation may only hold up to a certain percentage of active sites, beyond which further increases do not impact the catalyst's performance as the surface coverage of key reaction intermediates has already reached quasi-equilibrium. On the other hand, the present work does not take into account the Co-CO interactions, that were often speculated to induce surface mobility and reconstruction[2,45−49] and might thus significantly impact the NPs site distribution dependency on their size.

We employed the python package Wulffpack[50] to calculate the Wulff shape of *fcc*-Co crystals based on the nondefective surface energies reported in Table S1. A comparison between the Wulff and MC 10 nm Co NP is depicted in Figure 7. The Wulff construction assumes a crystal in the shape of a truncated octahedron (TO) that exposes predominantly the low-energy (111) surface, which alternates with smaller (100) surfaces. (110) and (311) surfaces, composed of B5−B and B5-A sites, respectively, are found at the intersections between (111)/(111) and (111)/(100) facets. The MC NP maintains the overall TO shape, but, unlike the Wulff constructed crystal, is characterized by significant irregularities. We additionally reported the site distribution of the 10 nm atomistic Wulff particle in Figure 6 (black data). We found that the Wulff crystal exposes a larger percentage of the 2B3 sites at the expense of B4 sites with respect to the MC particles. We additionally observe an increase of B5-A sites when comparing the Wulff and the MC NPs, while B5−B steps are present in similar proportions. Importantly, despite indications that they might significantly affect catalyst activity,[36] the Wulff construction does not include B6 sites, which largely arise from surface defects that this framework cannot reproduce. Furthermore, this approach can generate NPs with only the facets specified by the user, introducing a bias that our MC algorithm avoids. Lastly, the Wulff construction is size independent and hence not suitable to describe the structural evolution observed with increasing D_{Co}. This discussion makes it clear that the Wulff construction inherently fails to capture key features of NPs morphologies which are essential to understanding their catalytic properties. This underscores the need to move beyond the classical Wulff construction for describing metal NPs, an issue we have aimed to address in this study. Finally, we note that our approach may be

https://doi.org/10.1021/acs.jpcc.5c02777
J. Phys. Chem. C XXXX, XXX, XXX−XXX

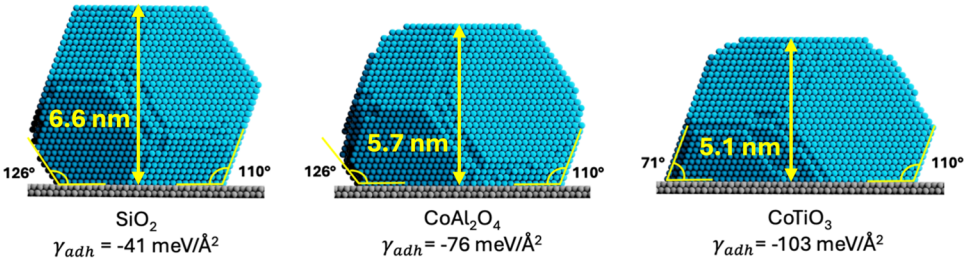

Figure 8. 8 nm Co NPs on supports with increasing adhesion energy.

unsuitable for simulating metal NPs at low temperatures. Under such conditions, the Metropolis criterion permits only energy-lowering moves, leading the system to become trapped in metastable states and preventing it from reaching the global energy minimum. However, this is of limited relevance for catalytic applications, which are typically conducted at higher temperatures.

3.3. Effect of the Support on Co NPs. Importantly, as our modeling relies solely on the energy assigned to each Co atom, we can elegantly include the effect of the support, as we just have to add the contribution of the adhesion energy between the support and the Co atoms binding to it. This has been done for three selected supports ranging roughly from noninteracting (SiO_2) to medium ($CoAl_2O_4$) and strongly interacting ($CoTiO_3$). We chose the 8 nm particles to highlight the differences in support effects, and the results are shown in the snapshots depicted in Figure 8 (see Figure S14 for frontal, side, and top views). As expected, with larger γ_{adh}, the NPs appear increasingly flattened on the support with their heights being 31 (6.3 nm), 28 (5.7 nm), and 25 (5.1 nm) atomic layers for the SiO_2-, $CoAl_2O_4$-, and $CoTiO_3$-supported particles, respectively. For the SiO_2- and $CoAl_2O_4$-supported NPs, the lower (111) and (100) surfaces are found at the interface with the support with contact angles (θ) equal to 110 and 126°, respectively. With increasing MSI, the lower (111) and (100) surfaces shrink, with the latter disappearing on the $CoTiO_3$ support, leading to the lower and upper (111) surfaces being at the interface with θ = 110 and 71°, respectively. Furthermore, as shown in Figure 9, increasing MSI also lowers the dispersion of the metal, since an increasing number of atoms is found at the Co-support interface rather than on the surface, even though the decrease in dispersion becomes less relevant with increasing D_{Co}. Interestingly, the overall site distribution of the Co NPs is largely unchanged, as shown in Figure 10. We observe, however, that, with stronger MSI, the NPs are characterized by a slightly larger presence of 2B3 sites at the expense of B4 sites. These results indicate that changing the MSI will presumably not alter the intrinsic activity of Co NPs as their effect on B5-A, B5−B, and B6 site concentrations is negligible. Van Etten et al. reported that changing MSI affects the concentration of some of the considered surface sites but that the most active ones are mostly unaffected, leading to insensitivity of the predicted TOF on changing support.[14] We reach the same conclusion, even though our models predict no significant impact of increasing the MSI on any of the considered surface sites. Lastly, in Figures S15 and S16, we present the comparison between the SiO_2-supported Co NPs exposing the (111) and (100) surfaces at the metal−support interface. We found that both the site distribution and the overall shape of the NPs are hardly affected by changing the Co facet in contact with the support.

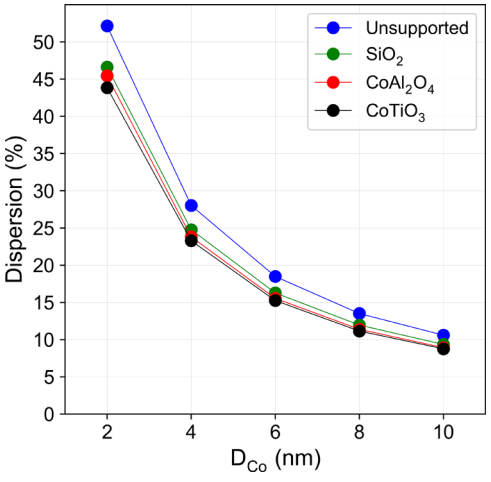

Figure 9. Dispersion (defined as N_{surf}/N_{tot}, where N_{tot} and N_{surf} are the total number of atoms and number of surface atoms, respectively) of Co NPs increases with increasing D_{Co} and changing support. Error bars have been omitted as they are negligibly small.

3.4. Stability and Surface Energies of Co NPs. The MSI, however, will have an influence on other properties, such as Co dispersion and stability against sintering. This is addressed in Figure 11a that depicts the surface energies of the various supported Co NPs as a function of size. These were obtained by dividing the total energy of the NPs by their surface areas, that were calculated as follows:

$$A_{NP} = \sum_i N_i A_i \tag{5}$$

$$\gamma = E_{NP}/A_{NP} \tag{6}$$

where A_{NP} is the surface area of the NP, N_i is the number of a specific type of site, A_i is its corresponding area, γ is the surface energy of the NP, and E_{NP} is the average of the total energies of the 40 lowest-energy structures obtained during each MC run. The calculated areas of the individual sites are 5.4, 6.2, 11.5, 8.8, and 11.8 Å^2 for the 2B3, B4, B5-A, B5−B, and B6 sites, respectively. For the calculation of γ for the supported particles, we did not include in E_{NP} the stabilization coming from the MSI, since this effect is independent and should thus be decoupled from the surface energy. All the surface energies are shown to decrease with increasing NP size since, as the NPs grow bigger, the concentration of low-coordinated corner and edge sites decreases, causing a stabilization of the surface, in agreement with several previous studies.[52−55] Even though γ changes notably across the different supports for the 2 nm NPs, it tends to converge to the same value with increasing D_{Co}. For the supported particles, γ slightly increases with increasing γ_{adh}, reflecting the mild increase of 2B3 at the expense of B4 sites

https://doi.org/10.1021/acs.jpcc.5c02777
J. Phys. Chem. C XXXX, XXX, XXX−XXX

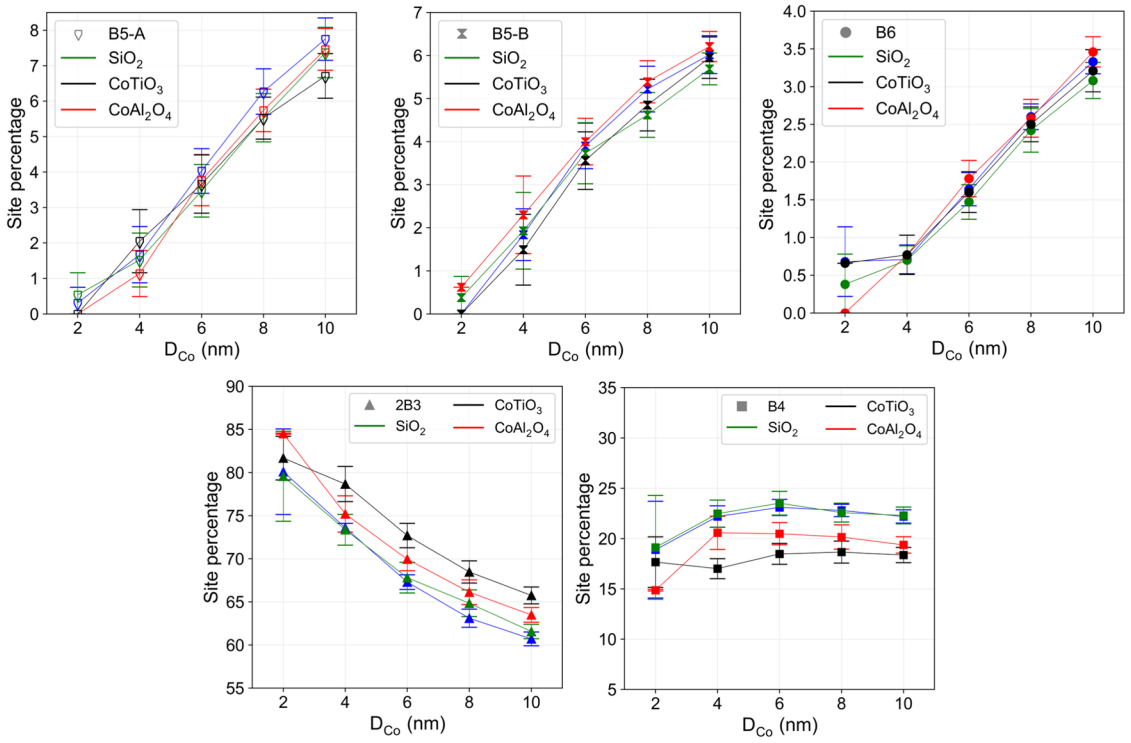

Figure 10. Site distribution analysis for unsupported, SiO_2-, $CoAl_2O_4$-, and $CoTiO_3$-supported Co NPs with increasing diameter.

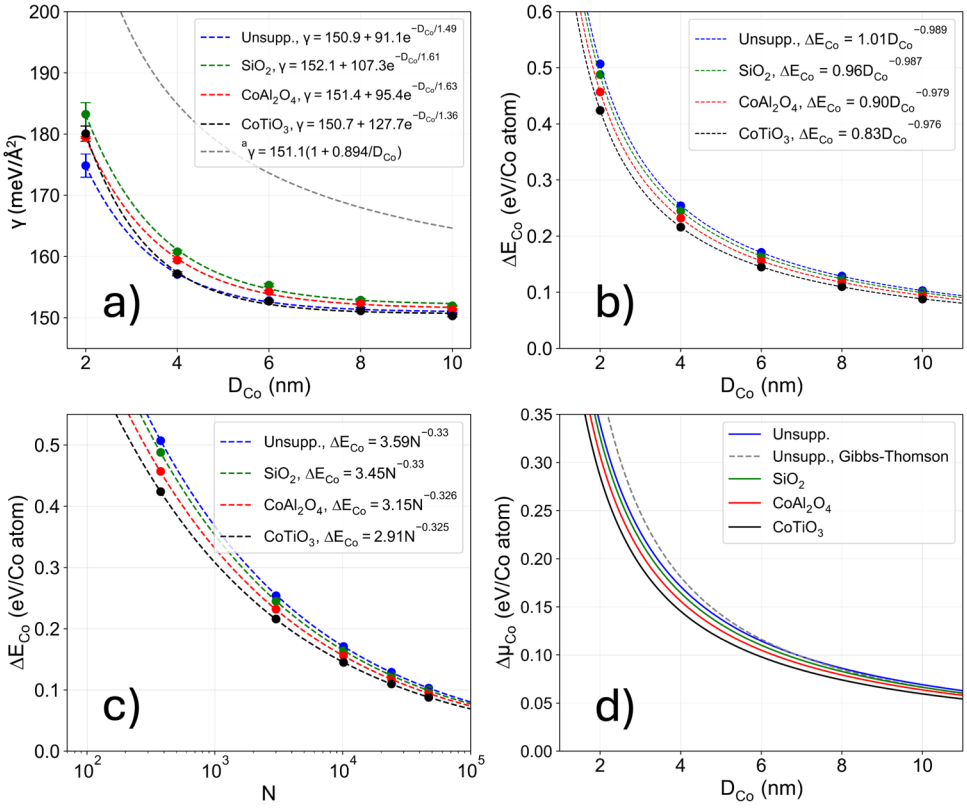

Figure 11. (a) Surface energies of Co NPs with increasing D_{Co} on different supports. (b) Average energy per atom ΔE_{Co} with respect to bulk Co with increasing D_{Co} and (c) with increasing number of atoms (N). (d) Chemical potential of the Co NPs $\Delta\mu_{Co}$ with increasing D_{Co}. The Gibbs−Thomson-derived $\Delta\mu_{Co}$ was calculated via eq 7 using the size-dependent surface energy of the free-standing particles. ([a]) Relation proposed by Rahmati et al.[51] to predict the γ of Co NPs.

reported in Figure 10. Nevertheless, γ for the supported particles is generally higher than for the unsupported ones, since the former exposes a large number of low-coordinated atoms at the edges of the metal−support interface. Regardless of the support,

https://doi.org/10.1021/acs.jpcc.5c02777
J. Phys. Chem. C XXXX, XXX, XXX−XXX

γ is shown to converge to a value of approximately 151 meV/Å^2, that is very close to the value of 157 meV/Å^2 (2.51 J/m^2) reported by Tyson et al.,[56] relative to the surface free energy of solid Co at 0 K extrapolated through a semitheoretical relation from liquid drop experiments at the melting temperature, thus suggesting that our DFT-based CN approach is adequate to estimate overall energies of Co NPs. We further report that γ converges on its bulk value from a relatively small D_{Co} = 6−8 nm. As shown in Section 3.1, NP growth is accompanied by an increase of steps and kinks that, due to low coordination, tend to increase the surface energy. This mitigates the impact on γ of the decrease in the concentration of edges and corners, effectively preventing it from diminishing further. In fact, even though the relation obtained for perfect cuboctahedral NPs proposed by Rahmati et al.[51] converges on a similar bulk γ as found from our models, it is shown to do so more slowly with increasing D_{Co}, likely because it does not take the relative increase of step and kink sites into account.

Figure 11b shows the energy with respect to bulk Co of the NPs on different supports normalized per Co atom (ΔE_{Co}). All the data could be fit by exponential functions with exponents slightly lower than −1 since the NP energy is a function of the surface-to-volume ratio, which is roughly proportional to R^{-1}. As expected, increasing γ_{adh} is shown to lower the NPs energy due to the stabilization arising from stronger adhesion on the support, even though this effect becomes less significant with increasing D_{Co}, due to the fact that the ratio between the number of Co atoms found at the interface with the support and the total decreases with particle size. The MSI mainly impact the preexponential factor of the function describing ΔE_{Co} that decreases from 1.01 eV/atom to 0.83 eV/atom between the unsupported and the Co-$CoTiO_3$ systems. Nevertheless, increasing adhesion strength also causes a slight increase in the exponent in the fitting functions.

Different fitting functions were used for ΔE_{Co} and γ due to their different physical origins. ΔE_{Co} reflects both surface and bulk contributions and scales with the surface-to-volume ratio (~1/D), justifying the use of a power-law fit, which matches the data closely. On the other hand, γ depends only on the local surface structure and lacks a well-defined scaling law. While its fit is more empirical, it reproduces the observed trend reasonably well and is useful, given the lack of well-established models that reproduce metal NPs surface energies in this size regime.

We further calculated the chemical potential of the Co NPs $\Delta\mu_{Co}$ with increasing D_{Co} via the following equation[54]

$$\Delta\mu_{Co} = \left(\frac{\partial(N \times \Delta E_{Co}(N)}{\partial N}\right)_{T,p} \quad (7)$$

The derivative described above was taken by substituting $\Delta E_{Co}(N)$ with the fitting functions reported in Figure 11c. Similarly to the case of ΔE_{Co}, increasing MSI lowers the $\Delta\mu_{Co}$, indicating a stabilization of the NPs. We additionally observe that the curves in Figure 11d become less steep with increasing γ_{adh}. This implies that the chemical potential difference between Co atoms in NPs of different sizes ($\Delta\mu_{NP}$), the thermodynamic driving force of sintering,[57] is reduced by stronger binding to the support. Thus, stronger adhesion on the support not only hinders sintering kinetically by increasing the diffusion barrier of NPs (or metal adatoms, in the case of Ostwald ripening sintering type) on the support,[58,59] but also retards the process from a thermodynamic standpoint by stabilizing smaller NPs to a larger extent than bigger ones. In Figure 11d, we additionally report in gray the $\Delta\mu_{Co}$ of unsupported NPs based on the classical Gibbs−Thomson relation:[60,61]

$$\Delta\mu_{Co} = \frac{2\gamma V_m}{R} \quad (8)$$

where V_m is the molar volume of Co, R is the radius of the NP, and γ is the surface energy of the free-standing NP shown in Figure 11a. Besides a slight overestimation of the $\Delta\mu_{Co}$ obtained through the Gibbs−Thomson relation in the low NP size range with respect to that obtained directly from our models of free-standing particles, the two curves yield very similar results. We note, however, that studies applying this relation, or any other model to calculate $\Delta\mu_{Co}$, usually lack an accurate estimation of the surface energy of the NPs, and either neglect the size dependency of γ[62−64] or rely on theoretical models based on ideal particle morphologies.[52,65] On the other hand, our method allows us to derive γ from NP models that take into account particle size, temperature, the presence of surface defects, and the influence of the support. We argue that the fact that our approach can consider all these effects simultaneously leads to a more realistic description of the structures and energetics of Co NPs and thus represents a step toward more accurate estimations of $\Delta\mu_{Co}$.

4. CONCLUSIONS

We have employed a paired DFT-MC approach to produce structural models of *fcc*-Co NPs taking into account particle size, temperature, and metal support interactions. We used a CN model to estimate the NPs energies, which was validated by DFT calculations of surface energies of ideal and defective facets. We have shown that our method includes important aspects that are classically neglected by the Wulff construction, namely, the presence of surface defects and the effects of particle size and temperature. With increasing NP size, the percentage of steps and kinks increases at the expense of close-packed surfaces. Previous computational studies reported the same behavior but predicted that a plateau of the site distribution would be reached for $D_{Co} \approx 5$ nm, which we do not observe. We argue that this structural evolution contributes to the observed size-dependent behavior of the TOF of Co catalysts, since steps and kinks are expected to showcase higher activity for CO dissociation. Importantly, our strategy allows for an easy inclusion of support effects within the model. This allowed us to observe the impact of changing MSI on the structure of the NPs. Increasing MSI led to flattening of the NPs on the support, but hardly affected the site distributions.

The values of γ and $\Delta\mu_{Co}$ of Co NPs obtained from our approach both decrease fast in the 2−6 nm d_{Co} range and near convergence with increasing particle size. The former mainly depends on the fraction of lower-coordinated atoms on the surface, while the latter depends on both γ and the surface/volume ratio. While previous attempts to estimate the energies of metal NPs were limited by approximations in the choice of γ, this study takes a different approach by considering realistic surface configurations of NPs, as our technique simultaneously accounts for complex effects, such as particle size, MSI, temperature, and defect formation. Our method thus improves the description of Co NPs energies with respect to the state of the art.

In conclusion, we successfully described the particle shape and site distributions of *fcc*-Co NPs, as a function of size and support interactions. We believe that this approach offers great

https://doi.org/10.1021/acs.jpcc.5c02777
J. Phys. Chem. C XXXX, XXX, XXX−XXX

potential for its application in future studies as it can be readily extended, e.g., by incorporating the effects of adsorbates.

■ ASSOCIATED CONTENT

Data Availability Statement

Home-made Monte Carlo code MC-Cluster available at https://github.com/T-136/MC-Cluster/tree/master or 10.35097/pqmqcrq4h47eucz5. Results of MC-simulations (lowest energy geometries and energies, as well as energies and CN-profile taken every 5×10^7 iterations for each run) for all the investigated particles found at 10.35097/rn0ygj9jwa7ggh91.

Supporting Information

The Supporting Information is available free of charge at https://pubs.acs.org/doi/10.1021/acs.jpcc.5c02777.

Additional tables, figures, computational and methodological details for surface energy calculations, U_{eff} calibration, ΔG^f calculations of Co-support compounds, adhesion energy calculations, convergence tests on the Monte Carlo simulations, CN model benchmarking on Co NPs, statistical analysis of the ensembles of unsupported NPs, analysis of the energetic diversity of the NPs with increasing temperature, snapshots of supported and unsupported NPs from three angles, and the comparison between SiO_2-supported Co NPs exposing the (111) and (100) facets at the interface (PDF)

Coordinates in xyz format and energies of all DFT-calculated structures (TXT)

■ AUTHOR INFORMATION

Corresponding Author

Felix Studt − *Institute of Catalysis Research and Technology, Karlsruhe Institute of Technology, 76344 Eggenstein-Leopoldshafen, Germany; Institute for Chemical Technology and Polymer Chemistry, Karlsruhe Institute of Technology, 76131 Karlsruhe, Germany;* orcid.org/0000-0001-6841-4232; Email: felix.studt@kit.edu

Authors

Enrico Sireci − *Institute of Catalysis Research and Technology, Karlsruhe Institute of Technology, 76344 Eggenstein-Leopoldshafen, Germany*

Tilman D. Grüger − *Institute of Catalysis Research and Technology, Karlsruhe Institute of Technology, 76344 Eggenstein-Leopoldshafen, Germany*

Philipp N. Plessow − *Institute of Catalysis Research and Technology, Karlsruhe Institute of Technology, 76344 Eggenstein-Leopoldshafen, Germany;* orcid.org/0000-0001-9913-4049

Dmitry I. Sharapa − *Institute of Catalysis Research and Technology, Karlsruhe Institute of Technology, 76344 Eggenstein-Leopoldshafen, Germany;* orcid.org/0000-0001-9510-9081

Complete contact information is available at: https://pubs.acs.org/10.1021/acs.jpcc.5c02777

Notes

The authors declare no competing financial interest.

■ ACKNOWLEDGMENTS

The authors gratefully acknowledge the financial support of the German Federal Ministry of Research, Technology and Space (BMFTR) within the CARE-O-SENE project (03SF0673). The authors acknowledge support by the state of Baden-Württemberg through bwHPC and the German Research Foundation (DFG) through grant no. INST 40/575-1 FUGG (JUSTUS 2 cluster, RVs bw17D011). Support from the Helmholtz Association is also gratefully acknowledged.

■ REFERENCES

(1) Bergero, C.; Gosnell, G.; Gielen, D.; Kang, S.; Bazilian, M.; Davis, S. J. Pathways to Net-Zero Emissions from Aviation. *Nat. Sustainability* **2023**, *6* (4), 404−414.

(2) Bezemer, G. L.; Bitter, J. H.; Kuipers, H. P. C. E.; Oosterbeek, H.; Holewijn, J. E.; Xu, X.; Kapteijn, F.; Van Diilen, A. J.; De Jong, K. P. Cobalt Particle Size Effects in the Fischer−Tropsch Reaction Studied with Carbon Nanofiber Supported Catalysts. *J. Am. Chem. Soc.* **2006**, *128* (12), 3956−3964.

(3) Prieto, G.; Martínez, A.; Concepción, P.; Moreno-Tost, R. Cobalt Particle Size Effects in Fischer−Tropsch Synthesis: Structural and in Situ Spectroscopic Characterisation on Reverse Micelle-Synthesised Co/ITQ-2 Model Catalysts. *J. Catal.* **2009**, *266* (1), 129−144.

(4) Yang, J.; Tveten, E. Z.; Chen, D.; Holmen, A. Understanding the Effect of Cobalt Particle Size on Fischer−Tropsch Synthesis: Surface Species and Mechanistic Studies by SSITKA and Kinetic Isotope Effect. *Langmuir* **2010**, *26* (21), 16558−16567.

(5) Herranz, T.; Deng, X.; Cabot, A.; Guo, J.; Salmeron, M. Influence of the Cobalt Particle Size in the CO Hydrogenation Reaction Studied by in Situ X-Ray Absorption Spectroscopy. *J. Phys. Chem. B* **2009**, *113* (31), 10721−10727.

(6) Fischer, N.; Van Steen, E.; Claeys, M. Structure Sensitivity of the Fischer−Tropsch Activity and Selectivity on Alumina Supported Cobalt Catalysts. *J. Catal.* **2013**, *299*, 67−80.

(7) Eschemann, T. O.; Lamme, W. S.; Manchester, R. L.; Parmentier, T. E.; Cognigni, A.; Rønning, M.; De Jong, K. P. Effect of Support Surface Treatment on the Synthesis, Structure, and Performance of Co/CNT Fischer−Tropsch Catalysts. *J. Catal.* **2015**, *328*, 130−138.

(8) Melaet, G.; Lindeman, A. E.; Somorjai, G. A. Cobalt Particle Size Effects in the Fischer−Tropsch Synthesis and in the Hydrogenation of CO2 Studied with Nanoparticle Model Catalysts on Silica. *Top. Catal.* **2014**, *57* (6−9), 500−507.

(9) Ralston, W. T.; Melaet, G.; Saephan, T.; Somorjai, G. A. Evidence of Structure Sensitivity in the Fischer−Tropsch Reaction on Model Cobalt Nanoparticles by Time-Resolved Chemical Transient Kinetics. *Angew. Chem.* **2017**, *129* (26), 7523−7527.

(10) Xiong, H.; Motchelaho, M. A. M.; Moyo, M.; Jewell, L. L.; Coville, N. J. Correlating the Preparation and Performance of Cobalt Catalysts Supported on Carbon Nanotubes and Carbon Spheres in the Fischer−Tropsch Synthesis. *J. Catal.* **2011**, *278* (1), 26−40.

(11) Rommens, K. T.; Saeys, M. Molecular Views on Fischer−Tropsch Synthesis. *Chem. Rev.* **2023**, *123* (9), 5798−5858.

(12) Van de Loosdrecht, J.; Botes, F. G.; Ciobîcă, I. M.; Ferreira, A.; Gibson, P.; Moodley, D. J.; Saib, A. M.; Visagie, J. L.; Weststrate, C. J.; Niemantsverdriet, J. W. Fischer−Tropsch Synthesis: Catalysts and Chemistry. In *Comprehensive Inorganic Chemistry II*; ELSEVIER, 2013; Vol. 7, pp 525−557.

(13) Agrawal, R.; Phatak, P.; Spanu, L. Effect of Phase and Size on Surface Sites in Cobalt Nanoparticles. *Catal. Today* **2018**, *312*, 174−180.

(14) Van Etten, M. P. C.; De Laat, M. E.; Hensen, E. J. M.; Filot, I. A. W. Unraveling the Role of Metal-Support Interactions on the Structure Sensitivity of Fischer−Tropsch Synthesis. *J. Phys. Chem. C* **2023**, *127* (31), 15148−15156.

(15) Van Etten, M. P. C.; Zijlstra, B.; Hensen, E. J. M.; Filot, I. A. W. Enumerating Active Sites on Metal Nanoparticles: Understanding the Size Dependence of Cobalt Particles for CO Dissociation. *ACS Catal.* **2021**, *11*, 8484−8492.

(16) Van Helden, P.; Ciobîcă, I. M.; Coetzer, R. L. J. The Size-Dependent Site Composition of FCC Cobalt Nanocrystals. *Catal. Today* **2016**, *261*, 48−59.

(17) Moodley, D.; Potgieter, J.; Moodley, P.; Crous, R.; van Helden, P.; van Zyl, L.; Cunningham, R.; Gauché, J.; Visagie, K.; Botha, T.; et al. Tuning the Active Sites of Supported Cobalt Fischer−Tropsch Catalysts to Enhance Efficiency for Hard Wax Production. *Catal. Today* **2025**, *454*, No. 115282.
(18) Pestman, R.; Chen, W.; Hensen, E. Insight into the Rate-Determining Step and Active Sites in the Fischer−Tropsch Reaction over Cobalt Catalysts. *ACS Catal.* **2019**, *9* (5), 4189−4195.
(19) Farris, R.; Neyman, K. M.; Bruix, A. Determining the Chemical Ordering in Nanoalloys by Considering Atomic Coordination Types. *J. Chem. Phys.* **2024**, *161* (13), No. 134114.
(20) Vega, L.; Aleksandrov, H. A.; Farris, R.; Bruix, A.; Viñes, F.; Neyman, K. M. Chemical Ordering in Pt-Au, Pt-Ag and Pt-Cu Nanoparticles from Density Functional Calculations Using a Topological Approach. *Mater. Adv.* **2021**, *2* (20), 6589−6602.
(21) Cheula, R.; Maestri, M.; Mpourmpakis, G. Modeling Morphology and Catalytic Activity of Nanoparticle Ensembles under Reaction Conditions. *ACS Catal.* **2020**, *10* (11), 6149−6158.
(22) Cioni, M.; Piane, M. D.; Polino, D.; Rapetti, D.; Crippa, M.; Irmak, E. A.; Van Aert, S.; Bals, S.; Pavan, G. M. Sampling Real-Time Atomic Dynamics in Metal Nanoparticles by Combining Experiments, Simulations, and Machine Learning. *Adv. Sci.* **2024**, *11* (25), No. 2307261.
(23) Spanò, G.; Ferri, M.; Cheula, R.; Monai, M.; Weckhuysen, B. M.; Maestri, M. Deciphering Size and Shape Effects on the Structure Sensitivity of the CO2Methanation Reaction on Nickel. *ACS Catal.* **2025**, *15*, 8194−8203.
(24) Dietze, E. M.; Plessow, P. N.; Studt, F. Modeling the Size Dependency of the Stability of Metal Nanoparticles. *J. Phys. Chem. C* **2019**, *123* (41), 25464−25469.
(25) Galanakis, I.; Papanikolaou, N.; Dederichs, P. H. Applicability of the Broken-Bond Rule to the Surface Energy of the Fcc Metals. *Surf. Sci.* **2002**, *511*, 1−2.
(26) Kitakami, O.; Sato, H.; Shimada, Y.; Sato, F.; Tanaka, M. Size Effect on the Crystal Phase of Cobalt Fine Particles. *Phys. Rev. B* **1997**, *56* (21), 13849−13854.
(27) Kresse, G.; Furthmüller, J. Efficiency of Ab-Initio Total Energy Calculations for Metals and Semiconductors Using a Plane-Wave Basis Set. *Comput. Mater. Sci.* **1996**, *6*, 15−50.
(28) Kresse, G.; Hafner, J. Ab Initio Molecular Dynamics for Liquid Metals. *Phys. Rev. B* **1993**, *47* (1), 558−561.
(29) Wellendorff, J.; Lundgaard, K. T.; Møgelhøj, A.; Petzold, V.; Landis, D. D.; Nørskov, J. K.; Bligaard, T.; Jacobsen, K. W. Density Functionals for Surface Science: Exchange-Correlation Model Development with Bayesian Error Estimation. *Phys. Rev. B* **2012**, *85* (23), No. 235149.
(30) Kresse, G.; Joubert, D. From Ultrasoft Pseudopotentials to the Projector Augmented-Wave Method. *Phys. Rev. B* **1999**, *59* (3), 1758−1775.
(31) Fiorentini, V.; Methfessel, M. Extracting Convergent Surface Energies from Slab Calculations. *J. Phys.: Condens. Matter* **1996**, *8*, 6525−6529.
(32) Saib, A. M.; Borgna, A.; van de Loosdrecht, J.; van Berge, P. J.; Niemantsverdriet, J. W. XANES Study of the Susceptibility of Nano-Sized Cobalt Crystallites to Oxidation during Realistic Fischer−Tropsch Synthesis. *Appl. Catal. A Gen* **2006**, *312* (1−2), 12−19.
(33) Qiu, C.; Odarchenko, Y.; Meng, Q.; Cong, P.; Schoen, M. A. W.; Kleibert, A.; Forrest, T.; Beale, A. M. Direct Observation of the Evolving Metal-Support Interaction of Individual Cobalt Nanoparticles at the Titania and Silica Interface. *Chem. Sci.* **2020**, *11* (48), 13060−13070.
(34) Dudarev, S. L.; Botton, G. A.; Savrasov, S. Y.; Humphreys, C. J.; Sutton, A. P. Electron-Energy-Loss Spectra and the Structural Stability of Nickel Oxide: An LSDAU Study. *Phys. Rev. B* **1998**, *57* (3), 1505−1509.
(35) Dietze, E. M.; Plessow, P. N. Predicting the Strength of Metal-Support Interaction with Computational Descriptors for Adhesion Energies. *J. Phys. Chem. C* **2019**, *123* (33), 20443−20450.
(36) van Hardeveld, R.; Hartog, F. The Statistics of Surface Atoms and Surface Sites on Metal Crystals. *Surf. Sci.* **1969**, *15*, 189−230.
(37) Swart, C. J. W. A Theoretical View on Deactivation of Cobalt-Based Fischer−Tropsch Catalysts; Ph.D. Thesis; University of Cape Town: Cape Town, 2008.
(38) Yang, L.; DePristo, A. E. On the Compact Structure of Small Fcc Metal Clusters. *J. Catal.* **1994**, *149*, 223−228.
(39) Methfessel, M.; Hennig, D.; Scheffler, M. Calculated Surface Energies of the 4d Transition Metals: A Study of Bond-Cutting Models. *Appl. Phys.* **1992**, *55*, 442−448.
(40) Zuo, Y.; Chen, C.; Li, X.; Deng, Z.; Chen, Y.; Behler, J.; Csányi, G.; Shapeev, A. V.; Thompson, A. P.; Wood, M. A.; Ong, S. P. Performance and Cost Assessment of Machine Learning Interatomic Potentials. *J. Phys. Chem. A* **2020**, *124* (4), 731−745.
(41) Petersen, M. A.; Van Den Berg, J. A.; Ciobîcă, I. M.; Van Helden, P. Revisiting CO Activation on Co Catalysts: Impact of Step and Kink Sites from DFT. *ACS Catal.* **2017**, *7* (3), 1984−1992.
(42) Liu, J. X.; Su, H. Y.; Sun, D. P.; Zhang, B. Y.; Li, W. X. Crystallographic Dependence of CO Activation on Cobalt Catalysts: HCP versus FCC. *J. Am. Chem. Soc.* **2013**, *135* (44), 16284−16287.
(43) Van Helden, P.; Van Den, J. A.; Petersen, M. A.; Van Rensburg, W. J.; Ciobîcă, I. M.; Van De Loosdrecht, J. Computational Investigation of the Kinetics and Mechanism of the Initial Steps of the Fischer−Tropsch Synthesis on Cobalt. *Faraday Discuss.* **2017**, *197*, 117−151.
(44) Rommens, K. T.; Gunasooriya, G. T. K. K.; Saeys, M. Key Role of CO Coverage for Chain Growth in Co-Based Fischer−Tropsch Synthesis. *ACS Catal.* **2024**, *14* (9), 6696−6709.
(45) Wilson, J.; De Groot, C. Atomic-Scale Restructuring in High-Pressure Catalysis. *J. Phys. Chem. A* **1995**, *99*, 7860−7866.
(46) Prieto, G.; Martínez, A.; Concepción, P.; Moreno-Tost, R. Cobalt Particle Size Effects in Fischer−Tropsch Synthesis: Structural and In Situ Spectroscopic Characterisation on Reverse Micelle-Synthesised Co/ITQ-2 Model Catalysts. *J. Catal.* **2009**, *266* (1), 129−144.
(47) Banerjee, A.; Van Bavel, A. P.; Kuipers, H. P. C. E.; Saeys, M. Origin of the Formation of Nanoislands on Cobalt Catalysts during Fischer−Tropsch Synthesis. *ACS Catal.* **2015**, *5* (8), 4756−4760.
(48) Banerjee, A.; Navarro, V.; Frenken, J. W. M.; Van Bavel, A. P.; Kuipers, H. P. C. E.; Saeys, M. Shape and Size of Cobalt Nanoislands Formed Spontaneously on Cobalt Terraces during Fischer−Tropsch Synthesis. *J. Phys. Chem. Lett.* **2016**, *7* (11), 1996−2001.
(49) Böller, B.; Ehrensperger, M.; Wintterlin, J. In Situ Scanning Tunneling Microscopy of the Dissociation of CO on Co(0001). *ACS Catal.* **2015**, *5* (11), 6802−6806.
(50) Rahm, J.; Erhart, P. WulffPack: A Python Package for Wulff Constructions. *J. Open Source Softw* **2020**, *5* (45), No. 1944.
(51) Rahmati, M.; Safdari, M. S.; Fletcher, T. H.; Argyle, M. D.; Bartholomew, C. H. Chemical and Thermal Sintering of Supported Metals with Emphasis on Cobalt Catalysts during Fischer−Tropsch Synthesis. *Chem. Rev.* **2020**, *120* (10), 4455−4533.
(52) Campbell, C. T.; Parker, S. C.; Starr, D. E. The Effect of Size-Dependent Energetics on Catalyst Sintering. *Science* **2002**, *298*, 811−814.
(53) Campbell, C. T. The Energetics of Supported Metal Nanoparticles: Relationships to Sintering Rates and Catalytic Activity. *Acc. Chem. Res.* **2013**, *46* (8), 1712−1719.
(54) Kang, S. B.; Lim, J. Bin.; Jo, D.; Nam, I. S.; Cho, B. K.; Hong, S. B.; Kim, C. H.; Oh, S. H. Ostwald-Ripening Sintering Kinetics of Pd-Based Three-Way Catalyst: Importance of Initial Particle Size of Pd. *Chem. Eng. J.* **2017**, *316*, 631−644.
(55) Van Steen, E.; Claeys, M.; Dry, M. E.; Van De Loosdrecht, J.; Viljoen, E. L.; Visagie, J. L. Stability of Nanocrystals: Thermodynamic Analysis of Oxidation and Re-Reduction of Cobalt in Water/Hydrogen Mixtures. *J. Phys. Chem. B* **2005**, *109* (8), 3575−3577.
(56) Tyson, W. R.; Miller, W. A. Sruface Free Energies of Solid Metals: Estimation from Liquid Surface Tension Measurements. *Surf. Sci.* **1977**, *62*, 267−276.

https://doi.org/10.1021/acs.jpcc.5c02777
J. Phys. Chem. C XXXX, XXX, XXX−XXX

(57) Campbell, C. T.; Mao, Z. Chemical Potential of Metal Atoms in Supported Nanoparticles: Dependence upon Particle Size and Support. *ACS Catal.* **2017**, *7* (12), 8460−8466.
(58) Dietze, E. M.; Abild-Pedersen, F.; Plessow, P. N. Comparison of Sintering by Particle Migration and Ripening through First-Principles-Based Simulations. *J. Phys. Chem. C* **2018**, *122* (46), 26563−26569.
(59) Plessow, P. N.; Sánchez-Carrera, R. S.; Li, L.; Rieger, M.; Sauer, S.; Schaefer, A.; Abild-Pedersen, F. Modeling the Interface of Platinum and α-Quartz(001): Implications for Sintering. *J. Phys. Chem. C* **2016**, *120* (19), 10340−10350.
(60) Johnson, C. A.; Bain, E. C. Generalization of the Gibbs-Thomson Equation. *Surf. Sci.* **1965**, *3*, 429−444.
(61) Plessow, P. N.; Campbell, C. T. Influence of Adhesion on the Chemical Potential of Supported Nanoparticles as Modeled with Spherical Caps. *ACS Catal.* **2022**, *12* (4), 2302−2308.
(62) Ouyang, R.; Liu, J. X.; Li, W. X. Atomistic Theory of Ostwald Ripening and Disintegration of Supported Metal Particles under Reaction Conditions. *J. Am. Chem. Soc.* **2013**, *135* (5), 1760−1771.
(63) Hu, S.; Li, W. X. Theoretical Investigation of Metal-Support Interactions on Ripening Kinetics of Supported Particles. *ChemNanoMat* **2018**, *4* (5), 510−517.
(64) Houk, L. R.; Challa, S. R.; Grayson, B.; Fanson, P.; Datye, A. K. The Definition of "Critical Radius" for a Collection of Nanoparticles Undergoing Ostwald Ripening. *Langmuir* **2009**, *25* (19), 11225−11227.
(65) Van Steen, E.; Claeys, M.; Dry, M. E.; Van De Loosdrecht, J.; Viljoen, E. L.; Visagie, J. L. Stability of Nanocrystals: Thermodynamic Analysis of Oxidation and Re-reduction of Cobalt in Water/Hydrogen Mixtures. *J. Phys. Chem. B* **2005**, *109* (8), 3575−3577.

https://doi.org/10.1021/acs.jpcc.5c02777
J. Phys. Chem. C XXXX, XXX, XXX−XXX